NANO · MICRO small
www.small-journal.com

High Resolution Membrane Structures within Hybrid Lipid-Polymer Vesicles Revealed by Combining X-Ray Scattering and Electron Microscopy

*Rashmi Seneviratne, Georgina Coates, Zexi Xu, Caitlin E. Cornell, Rebecca F. Thompson, Amin Sadeghpour, Daniel P. Maskell, Lars J. C. Jeuken, Michael Rappolt, and Paul A. Beales**

Hybrid vesicles consisting of phospholipids and block-copolymers are increasingly finding applications in science and technology. Herein, small angle X-ray scattering (SAXS) and cryo-electron tomography (cryo-ET) are used to obtain detailed structural information about hybrid vesicles with different ratios of 1-palmitoyl-2-oleoyl-sn-glycero-3-phosphocholine (POPC) and poly(1,2-butadiene-block-ethylene oxide) (PBd_{22}-PEO_{14}, M_s = 1800 g mol^{-1}). Using single particle analysis (SPA) the authors are able to further interpret the information gained from SAXS and cryo-ET experiments, showing that increasing PBd_{22}-PEO_{14} mole fraction increases the membrane thickness from 52 Å for a pure lipid system to 97 Å for pure PBd_{22}-PEO_{14} vesicles. Two vesicle populations with different membrane thicknesses in hybrid vesicle samples are found. As these lipids and polymers are reported to homogeneously mix, bistability is inferred between weak and strong interdigitation regimes of PBd_{22}-PEO_{14} within the hybrid membranes. It is hypothesized that membranes of intermediate structure are not energetically favorable. Therefore, each vesicle exists in one of these two membrane structures, which are assumed to have comparable free energies. The authors conclude that, by combining biophysical methods, accurate determination of the influence of composition on the structural properties of hybrid membranes is achieved, revealing that two distinct membranes structures can coexist in homogeneously mixed lipid-polymer hybrid vesicles.

1. Introduction

Vesicles have many applications from microreactors[1] and sensors,[2] to drug delivery vectors[3] and models for cell membrane research.[4] Lipids and amphiphilic block copolymers are common materials for the fabrication of synthetic or model membrane vesicles in the form of liposomes and polymersomes, respectively.[5] More recently, there has been significant interest in hybrid vesicles for technological applications that combine advantageous material properties from blended lipid and block copolymer components.[6]

Inclusion of membrane proteins within the vesicle membrane opens a range of potential applications, from carriers and bioreactors for drug delivery to sensors and artificial cells.[4a,7] Classically, membrane proteins have been reconstituted into liposomes because their membranes most closely resemble their native biomembrane environment.[8] However, phospholipid membranes are known to be chemically and structurally labile. For instance, the oxidation of the double

R. Seneviratne, G. Coates, P. A. Beales
School of Chemistry and Astbury Centre for Structural Molecular Biology
University of Leeds
Leeds LS2 9JT, UK
E-mail: p.a.beales@leeds.ac.uk

Z. Xu
School of Food Science and Nutrition
School of Chemistry and Astbury Centre for Structural Molecular Biology
University of Leeds
Leeds LS2 9JT, UK

The ORCID identification number(s) for the author(s) of this article can be found under https://doi.org/10.1002/smll.202206267.

DOI: 10.1002/smll.202206267

C. E. Cornell
Department of Bioengineering
University of California
Berkeley, CA 94720, USA

R. F. Thompson, D. P. Maskell
School of Molecular and Cellular Biology and Astbury Centre for Structural Molecular Biology
University of Leeds
Leeds LS2 9JT, UK

A. Sadeghpour, M. Rappolt
School of Food Science and Nutrition
University of Leeds
Leeds LS2 9JT, UK

L. J. C. Jeuken
Leiden Institute of Chemistry
Leiden University
PC Box 9502, Leiden 2300 RA, Netherlands

bonds of the fatty acid chains in an aerobic environment decreases membrane stability over time, resulting in leakage of contents by the formation of transitory pores and lipid aggregation. Unlike liposomes, polymersomes are more colloidally stable, robust, have a low permeability,[9] and can be functionalized to tune their properties.[3a] Polymersomes have been used for the encapsulation of molecules such as drugs,[3c,10] enzymes,[11] and DNA or RNA fragments[12] and for protein reconstitution, despite their difference in material properties from native membranes such as membrane fluidity and membrane thickness.[13]

However, polymer membranes are not an ideal solution for every application: the inherent biocompatibility and biofunctionality of liposomes[9] can be lacking in polymer vesicles. This is especially important for applications requiring protein reconstitution as specific lipid interactions are essential for many membrane proteins to retain functionality.[6b] Combining lipids and polymers into a hybrid vesicle is one potential solution to the challenges that arise from using pure systems and membrane proteins have been successfully reconstituted within them.[6b,14]

Due to their technological interest, numerous studies report on the physical properties of hybrid vesicles.[3c,6c,d,14b,15] Previous studies have shown that 1-palmitoyl-2-oleoyl-sn-glycero-3-phosphocholine (POPC) and poly(1,2-butadiene-block-ethylene oxide) (PBd-PEO) form well-mixed hybrid vesicles with no evidence of compositional heterogeneities on optical length scales.[15a,16] The favorable mixing of these components has been attributed to the similar Hildebrand solubility parameter of the lipid and amphiphilic block copolymer components,[17] that is, here PBd mimics the long acyl chains of a phospholipid, while PEO is hydrophilic like the phosphocholine head group.[18] PEO is also known to improve the pharmacokinetic properties of vesicles due to its strong interaction with the hydrating water layer that imparts a stealth effect by suppressing binding of opsonin proteins to its surface. This hinders the recognition of the vesicle as a foreign body by the immune system.[19] Hybrid vesicles containing lower molecular weight PBd-PEO polymer are more likely to form homogeneous, well-mixed hybrid vesicles.[16,20] Other studies have used PBd-PEO of different molecular weights to form membranes suitable for membrane protein reconstitution.[18,21]

Not all hybrid vesicles form homogeneous, well-mixed membranes. Phase-separated lipid-rich and polymer-rich domains have been reported in hybrid PBd-PEO-phospholipid vesicles, when the lipid components preferentially want to form more ordered membrane structures such as liquid-ordered or gel phase domains.[20b,22] While liquid-disordered phase lipids are reported to form homogeneous membranes with PBd-PEO polymers, such lipids, depending upon conditions, can phase-separate, when mixed with block copolymers with less chemically compatible hydrophobic chains, for example, PDMS-PEO.[23]

Understanding the relationship between structure and material properties is required for the informed design of vesicular properties, including properties required for successful reconstitution of membrane proteins. However, there are currently limited high resolution structures of these hybrid membranes. Here, we have performed an in-depth structural characterization of hybrid vesicles using cryo-transmission electron microscopy (cryo-TEM), including single particle analysis (SPA), cryo-electron tomograph (cryo-ET) and small-angle X-ray scattering (SAXS). This structural information of hybrid vesicles of POPC mixed with PBd_{22}-PEO_{14} (M_s = 1800 g mol^{-1}, >85% 1,2 addition) is used to determine how increasing polymer mole fraction affects the structure and membrane properties of the hybrid vesicles. Previous work on POPC/PBd_{22}-PEO_{14} hybrid systems has confirmed that all mixtures of these components form homogeneous membranes without heterogeneities or phase separation.[15a,16]

Cryo-TEM is ideally suited to determine the size and shape of vesicles[24] and, after post-acquisition computation, resolve high resolution 3D density maps.[25] Membrane thickness from cryo-TEM is usually measured between the outer edges of the contrast interfaces in images without consideration of the hydrophobic core.[24a,26] More detailed information can be obtained with SPA, which is more commonly used to determine structural features in proteins.[27] In SPA, multiple instances of the sample are imaged aligned, classified and combined to give a higher-resolution image[28] whereas cryo-electron tomography (cryo-ET) collects multiple images of the same specimen are taken at different angles, which can then be reconstituted into a 3D volume representing the same. Besides EM techniques, SAXS is an ensemble technique that has been used to confirm the size and shape of vesicle samples[29] and the average electron density profile (EDP) of lipid membranes,[29,30] unveiling, under optimized conditions, the membrane thickness with a precision of a few Ångströms.[31] However, the resultant scattering pattern is not always straightforward to model without some a priori structural information that constrain model fits to physically relevant solutions.[14b,25] This is because fitting SAXS data is model-dependent: the structural model cannot be stringently determined from the shape of the scattering profile. A plausible physical model needs to be determined by the user and several different structural models may satisfactorily fit the data. Therefore, electron microscopy images can provide valuable insight as the basis for an appropriate structural model to be applied.

While cryo-TEM and SAXS are powerful techniques on their own, their combined use offers several advantages as the information gained from one technique informs and helps optimize the other. For example, fully reconstructed 3D structures obtained using cryo-TEM have been used to obtain theoretical SAXS curves, which can be compared to experimental SAXS profiles.[25b] Therefore, the analysis of SAXS data can be refined with cryo-EM data to give the most probable ensemble structure.[25b] Here, we combine these techniques to provide high resolution membrane structures in hybrid vesicles and show the coexistence of two membrane thickness populations in hybrid systems. This bimodal bilayer thickness distribution, in what are reported to be well-mixed membranes, implies that structures of intermediate membrane thickness are energetically unfavorable.

2. Results and Discussion

2.1. Cryo-ET Images Show that Membrane Thickness Increases with Block Copolymer Composition

Large unilamellar vesicles (LUVs) with increasing PBd_{22}-PEO_{14} mole fraction were formed by extrusion (through 100 nm

track-etched pores) and mixed with colloidal gold, which act as fiducial markers for tomogram alignment. These fiducial markers are seen to be evenly dispersed throughout the sample and not localized to the vesicles and therefore are assumed to be passive and having no impact on the observed vesicle structures. From the tomogram, transmembrane line profiles of individual vesicles were collected in the same direction (inside to outside) to allow differentiation between the inner and outer membrane leaflets (data available in Section S1, Supporting Information). These line profiles were then averaged to find the electron intensity profile for a vesicle composition as shown in **Figure 1**. The statistics for the number of independent tomograms and vesicles used and the average number of intensity line profiles per vesicle for each vesicle composition are given in Table S6, Supporting Information. The electron intensity profiles were used to infer structural features in the bilayer, such as the membrane thickness from the full width half maximum (FWHM), and the hydrophobic core thickness using peak-to-peak distance. It should be noted here that these definitions vary from the standard definitions used for SAXS EDPs later on in this work, but gives best agreement between these two sets of data. These variations are likely due to subtle differences between the physics of the sample interaction and scattering of electrons and X-rays in these techniques.[32] We will give a detailed side-by-side discussion of electron intensity profiles (cryo-ET) and EDPs (SAXS) later in this manuscript to give clarity and resolution to these differences.

As the PBd_{22}-PEO_{14} mole fraction increases, the membrane thickness increases (Figure 1). A large increase in membrane thickness (from 57 to 78 and 83 to 97 Å) and hydrophobic core (from 36 to 50 and 53 to 66 Å) is observed between 25 mol% and 50 mol% and 75 mol% and 100 mol% PBd_{22}-PEO_{14}, respectively. From 0 mol% to 25 mol% PBd_{22}-PEO_{14} samples, we observe only a small increase in membrane thickness, suggesting that at low ratios, the polymer largely adapts to the intrinsic lipid bilayer thickness. In hybrid vesicles with >25 mol% PBd_{22}-PEO_{14}, the lipids instead appear to adapt to the thicker polymer membrane structure. 50 mol% and 75 mol% PBd_{22}-PEO_{14} compositions have a broad distribution in membrane thickness measurements, with some thicknesses comparable with that of a lipid membrane, and others close to that of a polymer membrane, as shown in Figure 1g.

The hydrophobic core thickness (peak-to-peak measurements) follows the same general trend as the membrane thickness: there is an increase in hydrophobic core thickness as the polymer fraction increases (see Section S2, Supporting Information). The hydrophobic core measurement delivers particularly useful information, when setting up an appropriate membrane model for fitting the SAXS pattern (see below).

The peak intensity values of individual vesicles were further used to determine, whether there was a transmembrane asymmetry in the different leaflets of the membrane (method and data available in Section S3, Supporting Information). Consistently significant differences in electron intensity between the inner and outer peaks would be indicative of membrane asymmetry. However, this fractional difference (relative difference between electron intensity) was less than 5% for all vesicle populations, including those composed of pure lipid or pure polymer, suggesting that none of the hybrid membranes had significant transverse compositional asymmetry. We attribute the slight electron intensity asymmetry that is observed in all vesicles to the curvature of the membrane, where the inner leaflet is slightly compressed when compared to that of the outer leaflet.

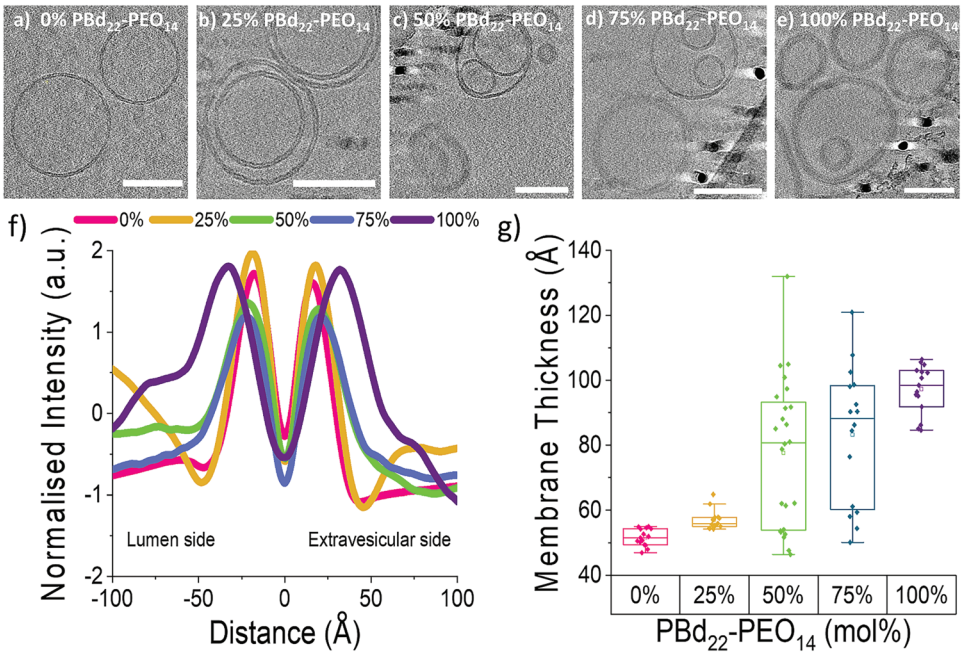

Figure 1. Electron intensity profiles (EIPs) of hybrid vesicle membranes obtained by cryo-ET. Cryo-ET images of a) POPC, b) 25%, c) 50%, d) 75%, and e) 100% PBd_{22}-PEO_{14} vesicle compositions (scale bar is 750 Å). The graphs show f) the average electron intensity profile across the vesicle membrane, and g) membrane thickness measurements (outer edges of contrast images in (a–e) of individual membranes within 0–100% PBd_{22}-PEO_{14} vesicle samples.

2.2. Two Populations of Different Membrane Thickness Are Observed in the Hybrid Vesicles

The membrane thicknesses shown in Figure 1 have a broad distribution for 50 mol% and 75 mol% PBd_{22}-PEO_{14} vesicles. When explored more closely, two groups of vesicles within these compositions begin to emerge: population 1 with a membrane thickness <60 Å and population 2 with a membrane thickness >70 Å, as shown in Figure 1g. The presence of two populations within each sample is significant to within a 95% confidence using a Tukey and Bonferroni ANOVA analysis. When compared with the pure systems, population 1 in both 50 mol% and 75 mol% PBd_{22}-PEO_{14} compositions has similar membrane thicknesses as 0% PBd_{22}-PEO_{14}, suggesting a thinner lipid-bilayer-like membrane structure, while measurement of population 2 vesicles infer a thicker polymersome-like membrane.

2.3. Coexisting Membrane Domains of Different Thickness Are not Observed in Individual Vesicles

Computational analysis was used to determine whether there were lateral domains of different thicknesses forming in the membrane of different vesicle compositions (see Section S4, Supporting Information).[33] The analysis compares the apparent membrane thickness along a section of a hybrid membrane with the bilayer thickness measurements of a pure lipid and pure polymer vesicle and computes the likelihood that a measurement in the hybrid membrane falls within the thickness distribution attributed to the pure lipid or pure polymer vesicle. The hybrid thickness measurements are sorted into thick, polymersome-like (>70 Å) and thin (<60 Å) membrane thickness categories.

The color maps overlaying the filtered images in **Figure 2** give the probability of the bilayer measurement corresponding to a thicker polymersome-like phase. Blue indicates 0% likelihood that the membrane is in the polymersome-like phase, while red indicates 100% likelihood that the membrane is in the polymersome-like phase. Our analysis occasionally assigns "thickness" to one leaflet only, rather than across two leaflets (bilayer), yielding anomalous results with the wrong color assignation. Values are discarded by visual inspection of the measurement lines of Canny-filtered (edge detection filter[34]) images, removing erroneous values. We analyzed between 20 and 25 vesicles for each hybrid composition: 25 mol% polymer (n = 20 thin membrane vesicles); 50 mol% polymer (n = 25, 15 thick membrane and 10 thin membrane); 75 mol% polymer (n = 24, 15 thick membrane and 9 thin membrane). For all hybrid vesicles analyzed, the r map shows that the membrane thickness is consistent throughout the vesicle. Therefore we find no evidence for coexistence of thick and thin membrane domains in the same vesicle. This suggests POPC and $PBd_{22}PEO_{14}$ are homogenously distributed within the membrane of vesicles in both thin and thick membrane vesicle populations.

2.4. Vesicle Diameters Correlate with Membrane Thickness for 75 mol% Polymer Hybrid Vesicles

All PBd_{22}-PEO_{14} samples were extruded using a membrane with a 100 nm pore size; average vesicles diameters from dynamic light scattering (provided in Section S5, Supporting

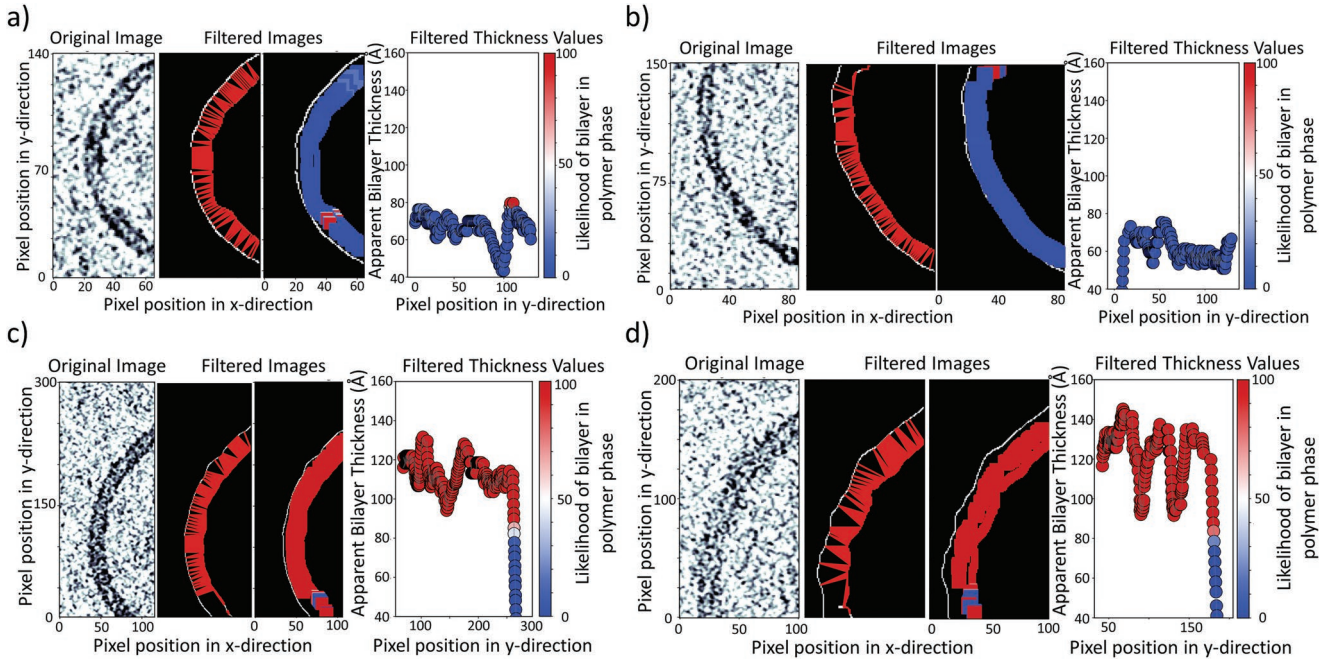

Figure 2. Hybrid vesicles have homogeneous membrane structures with no evidence of phase-separated domains. The original and Canny-filtered cryo-ET images with the measurement lines and determined phase as a color map of percentage likelihood the bilayer is in a polymersome-like phase of a) 25 mol% PBd_{22}-PEO_{14}, b) 50 mol% PBd_{22}-PEO_{14} (population 1), c) 50 mol% PBd_{22}-PEO_{14} (population 2), and d) 75 mol% PBd_{22}-PEO_{14} (population 2). Blue indicates 0% likelihood that membrane is in polymersome-like phase, while red indicates 100% likelihood that membrane is in polymersome-like phase.

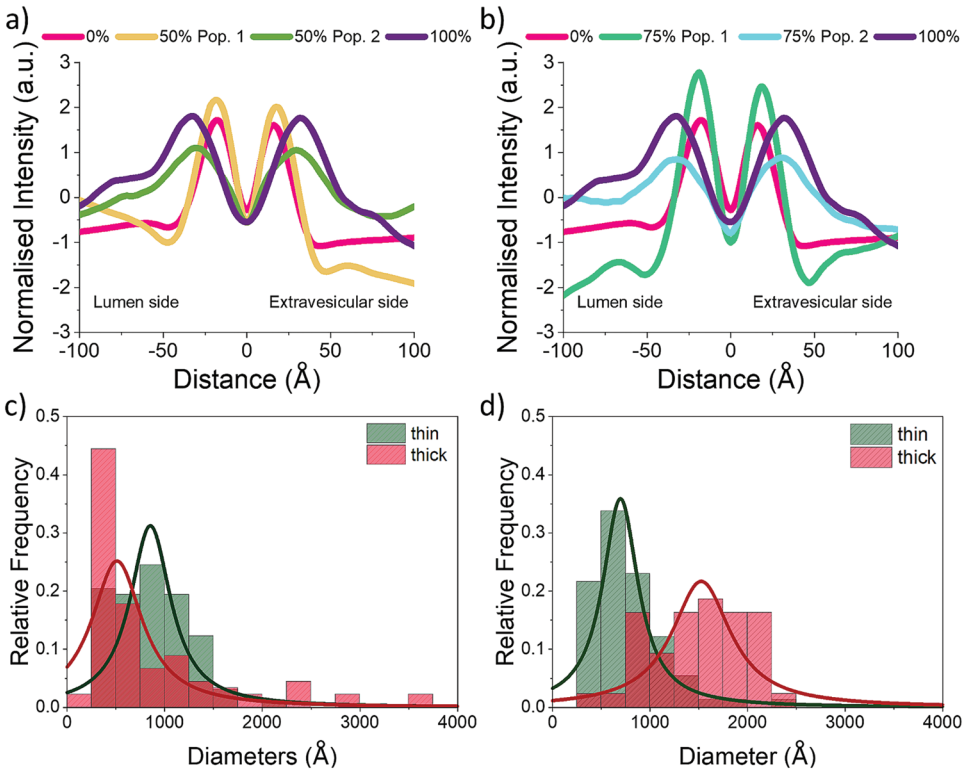

Figure 3. Two distinct membrane populations are observed at some hybrid vesicle compositions. Electron intensity profiles of 0%, 100% and population 1 and 2 of a) 50 mol% and b) 75 mol% PBd_{22}-PEO_{14} vesicle compositions. Population 1 (Pop. 1) of both 50 mol% and 75 mol% compositions has a profile similar to 0% indicating a thin membrane, while population 2 (Pop. 2) of both compositions is a thick membrane. The histograms of the vesicle diameters of the thick and thin populations in c) 50 mol% and d) 75 mol% PBd_{22}-PEO_{14}.

Information) and visual observation of cryo-TEM images indicate that the vesicles have a monomodal size distribution with average diameters >100 nm. We have previously reported detailed DLS data for hybrid vesicles of the compositions studied here.[15b] Initially DLS shows there is a small decrease in vesicle diameter between 0 mol% and 25 mol% PBd_{22}-PEO_{14} samples (131 nm, PDI 0.106 and 103 nm, PDI 0.120, respectively), and then the vesicle diameters increase with increasing PBd_{22}-PEO_{14} fraction to 141 nm (PDI 0.097) in the 100 mol% PBd_{22}-PEO_{14} sample. 50 mol% PBd_{22}-PEO_{14} sample had a high PDI of 0.236, suggesting that this sample was significantly more polydisperse than the other compositions.

As tomography has shown that there are two bilayer thickness populations in 50 mol% and 75 mol% PBd_{22}-PEO_{14} samples, the thickness might be related to the vesicle diameter (i.e., curvature), since $\kappa \propto d^2$, where κ is the membrane bending rigidity and d is the membrane thickness.[9a,35] To test this, vesicle diameter measurements were taken for every vesicle across 5 tomograms (188 vesicles in 50 mol% PBd_{22}-PEO_{14} and 117 vesicles in 75 mol% PBd_{22}-PEO_{14}) and categorized into thin or thick bilayer populations based on visual inspection.

As the difference between the membrane thickness of a thick and thin population is quite large, visual sorting is possible. The histograms in **Figure 3**c,d show the fraction of vesicles of thick or thin membrane thickness sorted by size. Upon first inspection, thin and thick membranes appear to coincide with smaller or larger vesicles in 50 mol% PBd_{22}-PEO_{14} samples. However further analysis shows that this difference is not statistically relevant ($p > 0.1$; Tukey & Bonferroni ANOVA). As shown in Figure 3c, the reason for the perceived difference is the presence of a large number of small vesicles with thick bilayer measurements. In contrast, thin membranes do significantly correlate with smaller vesicles and thicker membranes with larger vesicles in the 75 mol% PBd_{22}-PEO_{14} sample ($p < 0.05$; Tukey & Bonferroni ANOVA) as no small vesicles with thick membranes were observed. These observations are consistent with vesicle size being dictated by the higher bending rigidity of the vesicle population with thicker membranes.

2.5. Cryo-ET Results Refine the Ensemble Analysis of SAXS Data

Figure 4 shows that as the polymer mole fraction increases, that the scattering intensity increases in the SAXS patterns at low scattering vector q values (<0.08 $Å^{-1}$; for the definition of q see Section 4: Experimental Section). We note that as long as no highly resolved diffraction pattern is present (no underlying ordered structure exists), the SAXS pattern must be modelled in order to retrieve structural membrane information.[25a] Therefore, when no contribution from a structure factor is given, the SAXS profiles can be fitted with a form factor contribution alone. The form factor contributions applied were adapted from a Gaussian-based model described previously.[36] The Fourier transformed Gaussian-based real space EDPs models result in

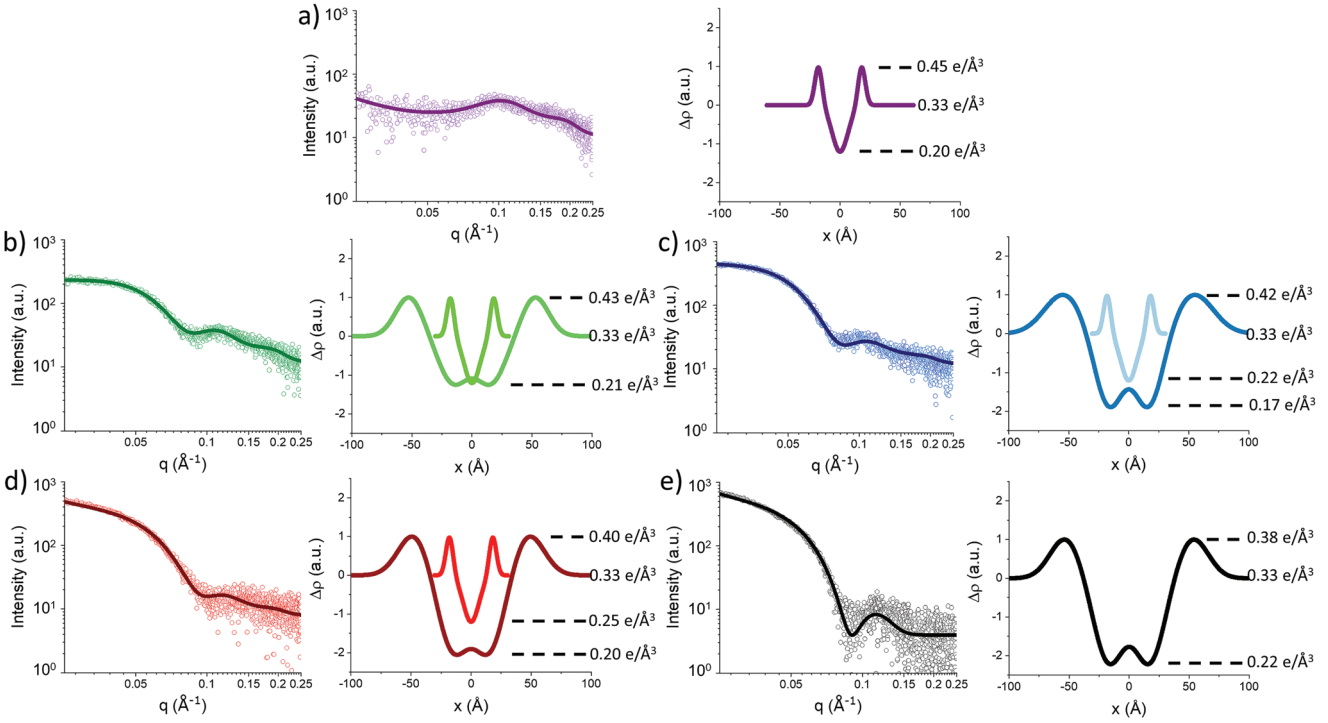

Figure 4. Membrane electron-density profiles (EDPs) of hybrid vesicles from SAXS using fitting models refined by cryo-ET data. Fitted SAXS profiles of a) 0%, b) 25 mol%, c) 50 mol%, d) 75 mol%, and e) 100% PBd_{22}-PEO_{14} and resultant electron density profiles. Thin and thick membrane populations were found in PBd_{22}-PEO_{14} hybrid vesicle samples, which agrees with the results obtained from cryo-ET. For pure POPC vesicles (a), a small but not neglectable scattering contribution stemming from intraluminal vesicles was additionally fitted (see details, Section S11, Supporting Information).

Equations (1) and (2) described below. By using results from cryo-ET, physically relevant models were developed. We note that the vesicles used for SAXS analysis were dilute (6.57 mM) and displayed a PDI < 0.25 from Dynamic Light Scattering (Section S5, Supporting Information).

Tomography has shown 50 mol% and 75 mol% PBd_{22}-PEO_{14} samples contain a thick and thin membrane populations. Therefore, SAXS patterns of these samples were fitted with models based on coexistence of two vesicle populations with thin membranes (F_{thin}) and thick membranes (F_{thick}).

For thin membranes, a 3-Gaussian form factor (F_{thin}) model is applied:[36a,37]

$$F_{thin}(q) = \sqrt{2\pi}\left(2\sigma_H \exp\left(-\frac{\sigma_H^2 q^2}{2}\right)\cos(qz_H) - \sigma_C \rho_R exp\left(-\frac{\sigma_C^2 q^2}{2}\right)\right) \quad (1)$$

where two Gaussians are used to represent polar headgroups at $\pm z_H$ and one Gaussian to model the methyl trough region at the bilayer midplane. The widths of these Gaussians are given by σ_H and σ_C, respectively. The ratio of the headgroup amplitude against the negative methyl group amplitude is the minimum to maximum electron density contrast, given as $\rho_R = \rho_C/\rho_H$.

To account for the broad hydrophobic core observed using tomography of samples for pure polymer membranes (PBd_{22}-PEO_{14}), a 4-Gaussian form factor F_{thick} was applied:

$$F_{thick}(q) = \sqrt{2\pi}\left(2\sigma_H \exp\left(-\frac{\sigma_H^2 q^2}{2}\right)\cos(qz_H) - 2\sigma_C \rho_R \exp\left(-\frac{\sigma_C^2 q^2}{2}\right)\cos(qz_C)\right) \quad (2)$$

where the broad hydrophobic core region is represented by two Gaussians at $\pm z_C$ with equal widths of σ_C and the position of the polar groups are given also by two Gaussians at $\pm z_H$ with equal widths of σ_H. The minimum to maximum electron density contrast here is given by $\rho_R = \rho_C/\rho_H$. Adding further fitting parameters (additional Gaussian distributions for the headgroup region) for the SAXS model for the thick membrane model (Equation (2)) did not statistically improve the fits (see Section S8, Supporting Information).

A single model was used to fit the pure lipid and polymer systems (the 3 Gaussian and 4 Gaussian functions of Equations (1) and (2), respectively). However, for the hybrid POPC-PBd_{22}-PEO_{14} membranes, a combination of the two models was required to account for contributions from both membrane structures. Led by the measurements obtained using cryo-ET, two models were fitted to the hybrid membranes resulting in both thick (Equation (2)) and thin (Equation (1)) membrane EDPs for each hybrid vesicle sample. For hybrid samples, a weighting factor, w, was applied for the fraction of the thick membrane vesicles in the hybrid sample (with $(1 - w)$ indicating the fraction of thin membrane vesicles):

$$F_{total}^2 = (1-w)\,F_{thin}^2 + w\,F_{thick}^2 \quad (3)$$

The output gives the superposition of two EDPs, which correspond to the thin membrane and thick membrane vesicles within the mixtures. Finally, the scattered intensity was fitted by the equation:

$$I(q) = F(q)^2/q^2 \quad (4)$$

with $F(q)$ being the total form factor as described in Equation (3) and the $1/q^2$ the Lorentz correction applied for planar structures.[36a,37]

While in the thin membrane vesicles, the EDP appears practically unchanged with increasing PBd_{22}-PEO_{14} mole fraction, in the thick membrane vesicles the bilayer thickness as well as the relative trough depth increases slightly ($\rho_R = \frac{\rho_C}{\rho_H}$ with ρ_H set to unity; see Table S5, Supporting Information). Figure 4 shows that initially the electron density ratio between hydrophobic core minima and hydrophilic electron density maxima is the smallest at 25 mol% PBd_{22}-PEO_{14} (Figure 4b). This ratio increases as the polymer fraction in the sample increases (Figure 4c,d). Since the electron density of the POPC head-group region is clearly bigger than in the PEO region, the observed trend can be explained. Note, on an absolute electron density scale the phosphate-group in POPC accounts for 0.45 e/Å^3[38] and compares to 0.38 e/Å^3 as estimated for an oxygen-rich PEO region. Further, to help with the relative EDP scale in Figure 4, the water density is 0.33 e/Å^3 and the methyl trough pure PC vesicles in the fluid phase is 0.20 e/Å^3.[38] For the pure polymersomes we estimate the head-group electron density to be 0.38 e/Å^3, which allows a rough estimate of the hydrophobic core electron density minimum to about 0.22 e/Å^3. Thus, the observed trend in ρ_R confirms that lipids are present in the thick membranes of the hybrid vesicles, and as the lipid fraction in the entire sample decreases, their presence in the thick membranes also decreases.

The percentage of thin and thick membranes in each sample was also calculated (see parameter w in Equation (3)) and compared to the fractions of thin and thick membranes found from cryo-ET images as shown in **Table 1**. Although cryo-ET showed no thick membrane population in 25% PBd_{22}-PEO_{14} hybrid vesicles, SAXS indicates that the two membrane populations also coexist within this hybrid composition. Overall, the fraction of thin membranes in each composition decreased as the polymer mole fraction increased, from 56% in the 25 mol% PBd_{22}-PEO_{14} sample to 15% in the 75 mol% PBd_{22}-PEO_{14} sample. As SAXS is an ensemble technique with high statistics, (10^{10} vesicles), compared to the low statistics of analyzing individual in cryo-ET images, (10^2 vesicles), the population fraction analysis is more accurately obtained from the SAXS data. However, the cryo-ET data was essential for determination of the SAXS fitting models used.

Table 1. The fractions of thin and thick membranes in POPC/PBd_{22}-PEO_{14} hybrid vesicle compositions found by cryo-ET and SAXS analysis.

PBd_{22}-PEO_{14} (mol%)	Cryo-ET		SAXS	
	Thin membrane (%)	Thick membrane (%)	Thin membrane (%)	Thick membrane (%)
0	100	0	100	0
25	100	0	56	44
50	58	42	25	75
75	63	36	15	85
100	0	100	0	100

2.6. Comparing Results from Cryo-ET, SAXS, and SPA Provides Deeper Insight into Hybrid Membrane Structures

To further support the SAXS fits and interpretation, SPA was used to obtain and group together multiple cryo-TEM projection images of 0%, 50%, and 100% PBd_{22}-PEO_{14} hybrid vesicles to give a high-resolution image of sections of membrane for each sample as shown in **Figure 5**.

A fast Fourier transform (FFT) of 10 cryo-ET images resulted in a scattering pattern similar to the SAXS scattering curves (see Section S6, Supporting Information). These FFT patterns were also fitted with either the 3-Gaussian model (Equation (1)) for thin membranes or the 4-Gaussian model (Equation (2)) for thick membranes to give an electron intensity profile of the membrane that can be compared to the electron density and intensity profiles from SAXS and cryo-TEM techniques.

We can now compare electron density and electron intensity profiles obtained from SAXS, cryo-ET, and SPA (**Figure 6**). A quantitative analysis using feature positions was carried out to compare these profiles directly: peak-to-peak measurements were taken from all electron profiles to determine whether the data acquired in the SAXS, cryo-ET and FFT of cryo-ET images and SPA correspond to the same structure.

Comparing the pure POPC lipid profiles, the peak-to peak positions from both SAXS, cryo-ET, FFT and SPA have excellent correspondence, where peak positions are closely aligned as shown by Figure 6a–d. In the SAXS profile, the peak-to-peak distances in POPC lipid membranes is 36 Å, while for the cryo-ET profile, the peak-to-peak distance is 34 Å (see Section S7, Supporting Information). The FFT and SPA profiles give

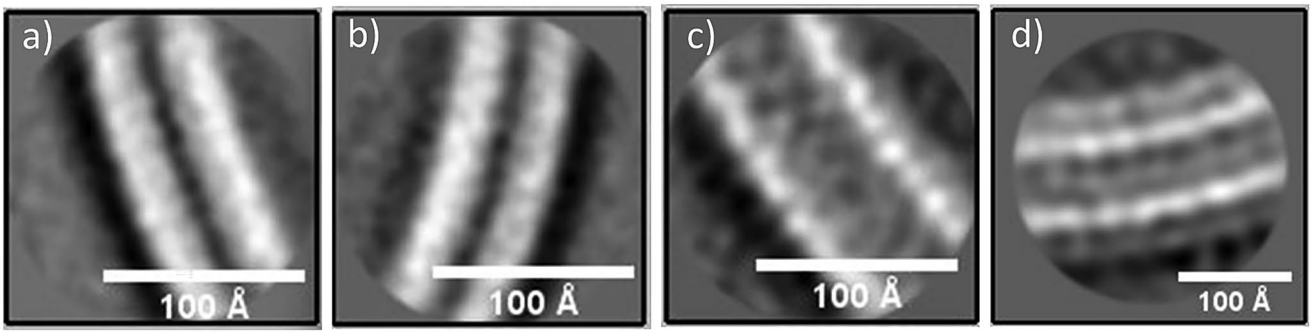

Figure 5. Single particle analysis of electron micrographs reveals detailed membrane structure. Cryo-EM SPA images of a) POPC, 50 mol% PBd_{22}-PEO_{14}, b) population 1, c) population 2 (thin and thick, respectively), and d) 100% PBd_{22}-PEO_{14} vesicle compositions.

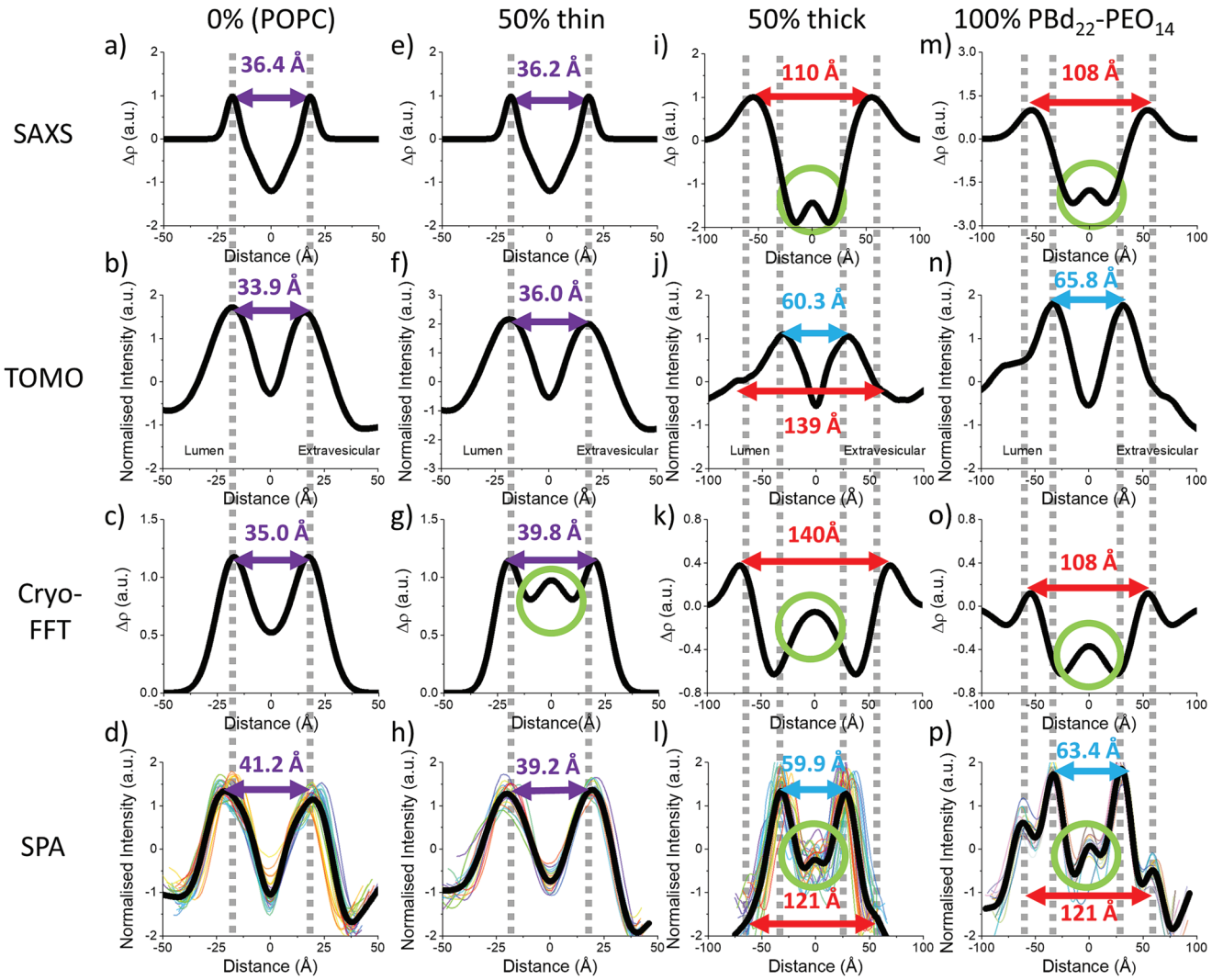

Figure 6. Correlating membrane structural features across the different SAXS and electron microscopy analyses. In 0 mol% PBd_{22}-PEO_{14} membranes, there is excellent correspondence between the a) SAXS electron density profile and the b) cryo-ET electron intensity profile, as well as the electron profiles resulting from c) FFT analysis of the cryo-ET images and d) SPA. In the thin population of 50 mol% PBd_{22}-PEO_{14} vesicles there is also excellent correspondence in peak-to-peak distances between the e) SAXS electron density profile and the f) cryo-ET electron intensity profile, as well as electron profiles resulting from g) FFT analysis of the cryo-ET images and h) SPA. Although for the thick 50 mol% PBd_{22}-PEO_{14} membranes, the i) SAXS electron density profiles do not correspond with j) cryo-ET electron intensity profiles. However, the k) FFT analysis of the cryo-ET images results in a profile that has excellent correspondence to (i). Further analysis with l) SPA gives a result that combines some of the features seen in both SAXS and cryo-ET (i,j) profiles, including a higher density peak in the hydrophobic core region indicated by the green circle. Like thick 50 PBd_{22}-PEO_{14} membranes, 100 mol% PBd_{22}-PEO_{14} membrane m) SAXS electron density profiles do not correspond with n) cryo-ET electron intensity profiles. However, o) FFT analysis of the cryo-ET images results in a profile that has excellent correspondence to (m). Further analysis with p) SPA gives a result that combines the features seen in both SAXS and cryo-ET (m,n) profiles including a higher density peak in the hydrophobic core region indicated by the green circle.

peak-to-peak measurements of 35 and 41 Å, respectively. All these measurements are comparable to the peak-to-peak and membrane thickness measurements of POPC lipid membranes found previously using SAXS and cryo-TEM: in SAXS, the peak-to-peak distance was estimated to be ≈38 Å,[36a,37,39] while measurements of cryo-TEM images gives a membrane thickness of 37 Å.[24a]

Both SAXS and cryo-ET reveal two bilayer populations within the 50 mol% PBd_{22}-PEO_{14} hybrid vesicles, one population presenting a thinner membrane <65 Å (Figure 6e–h), and the other with a thicker membrane >65 Å (Figure 6i–l). For thin membranes (<65 Å) of 50 mol% $PBd_{22}PEO_{14}$ vesicles, the peak-to-peak positions from both SAXS, cryo-ET, FFT and SPA also have excellent correspondence. Peak positions are closely aligned as shown by Figure 6e–h. In the SAXS profile, the peak-to-peak distances for the thin membranes are 36 Å, while for the cryo-ET profile, the peak-to-peak distance is 36 Å. The FFT and SPA profiles give peak-to-peak measurements of 40 and 39 Å, respectively. The FFT profile in Figure 6g also shows a small electron dense peak within the center of the trough region, potentially indicative of homogenous hybrid membranes as well as interdigitation within these membranes. As

previous studies have shown well mixed hybrid vesicles form from POPC/$PBd_{22}PEO_{14}$ mixtures, polymers present in both the inner and outer bilayer leaflets of these thin membranes would tangle to reduce exposure of their hydrophobic region to water. This region would then have a higher electron density due to interdigitation, than if the polymer leaflets were completely segregated.

There is a significant disparity between the appearance and peak-to-peak measurements between the SAXS EDP and the electron intensity profile obtained by cryo-ET for the thick membranes in the 50 mol% hybrid sample (Figures 6i,j, respectively). The SAXS profile suggests that the thick membrane population has a peak-to-peak thickness of 108 Å, while cryo-ET suggests a measurement of 60 Å, but with a shoulder contribution at about 130 Å. For this reason, a fit to our SAXS data with a split head-group contribution was tried (cf. Figure 6p), but the resulting 6-Gaussian model was not able to statistically improve our SAXS pattern fits (see Point S9, Supporting Information). Thus, the EM derived EIPs and SAXS model EDPs are not one to one comparable. That is, the peak-to-peak distance found in SAXS (108 Å) lies somewhere in between the two peak-to-peak values as found for SPA data (65 and 121 Å; Figure 6p). We interpret the two peaks in the SPA images to reflect the hydrophilic/hydrophobic interface (oxygen-dense interface) and the middle of the PEO corona (inner and outer peaks, respectively). In contrast, for the hydrophobic core agreement between SAXS and SPA EDPs is reached. The small electron dense peak within the center of the trough region (Figure 6i,k) is potentially indicative of interdigitation within thick 50 mol% $PBd_{22}PEO_{14}$ membranes. We note that cryo-ET data most probably misses this detail due to its lower resolution, when compared to SPA data (Figure 6n versus Figure 6p). The FFT analysis of the cryo-ET data leads to a similar membrane thickness as determined from the SAXS analysis, indicative that the same information is present in both sets of data. However, the reciprocal space analysis appears more sensitive to the outer PEO corona than the direct real space analysis of the cryo-ET images, where only a diffuse shoulder in the electron intensity is seen at these larger membrane thicknesses (Figure 6o versus Figure 6p).

The electron intensity profile resulting from SPA in Figure 6l combines features of the results seen in SAXS, cryo-ET, and FFT analysis. The SPA profile in Figure 6l has an inner peak-to-peak distance of 60 Å, which is very well comparable to cryo-ET results of 60 Å, and aligns with the hydrophobic core region (56 Å) in the SAXS profile (its borders are determined by the zero-point positions of the profiles). The SPA profile also potentially has two slight shoulders at approximately ±60 Å, which aligns with the peaks at ±55, ±70 and ± 70 Å seen in SAXS, FFT and cryo-ET profiles, respectively. Again, also at this concentration, the 4-Gaussian model used for thick 50 mol% PBd_{22}-PEO_{14} membranes does not account for these two additional positive electron density contributions in this structural region, which is why this particular feature is not reproduced in the SAXS data.

Similar differences are seen when evaluating the profiles of 100 mol% $PBd_{22}PEO_{14}$ membranes. Again, the SAXS data indicates much larger peak-to-peak distances compared to the cryo-ET profiles (108 and 66 Å, respectively), as seen in Figure 6m,n. As shown by Figure 6m,o, the peak-to-peak distance in the profile from the FFT corresponds to the peaks found from the SAXS scattering curves (108 Å from both techniques). A closer inspection of the SAXS and FFT also reveals a small electron dense peak in the center of the trough region, within the hydrophobic core. Again, this suggests that the information collected by SAXS is present in the cryo-ET images, but it is too noisy to be clearly resolved by our real space analysis of these images. The SPA profile of 100 mol% PBd_{22}-PEO_{14} in Figure 6p also shows a small electron dense peak within the center of the trough region. Comparing the SPA profile of thick membranes, this central peak has a greater intensity in 100 mol% $PBd_{22}PEO_{14}$ membranes than in thick 50 mol% $PBd_{22}PEO_{14}$ membranes. As this peak appears indicative of interdigitation within the membranes, perhaps the low peak intensity seen in the thick 50 mol% $PBd_{22}PEO_{14}$ membrane profile is due to an increased free volume in the hydrophobic core of these membranes due to the presence of shorter lipid molecules, reducing the extent of polymer interdigitation in the membrane mid-plane.

In Figure 6m the hydrophobic core region in the SAXS EDP (59 Å) corresponds with the inner peak-to-peak distance in cryo-ET and SPA profiles in Figures 6n,p (66 and 63 Å, respectively). Previously the hydrophobic core region for a similar polymer, PBd_{23}-PEO_{16}, was simulated to be 63 Å.[26b] Although the PBd_{23}-PEO_{16} polymer used in the previous study is slightly larger than PBd_{22}-PEO_{14} used here, there is good agreement between these previous simulations and our experimental peak to peak measurements from cryo-ET and SPA.

The cryo-ET profile in Figure 6n also shows a shoulder forming on the outer edges of these peaks at approximately ±80 Å. Although the position of this shoulder does not align with the outer peak at ±59 Å in the SPA profile, Figure 6p, this outer peak in the SPA profile is directly between the peak and shoulder positions in the cryo-ET profile. The same observation can be made when comparing the SAXS profile with the cryo-ET profile, where the SAXS peak position at ±54 Å is directly between the peak and shoulder in the cryo-ET profile. As mentioned, the 4-Gaussian model, used here for 100 mol% PBd_{22}-PEO_{14} membranes, does not account for these two additional positive electron density contributions in this structural region, which is why this particular feature cannot be reproduced, and may require application of an asymmetric membrane model. Comparing the SPA profile of thick membranes, these outer peaks have a greater intensity in 100 mol% $PBd_{22}PEO_{14}$ membranes than in thick 50 mol% $PBd_{22}PEO_{14}$ membranes. The lower intensity of the outer peaks in the thick 50 mol% $PBd_{22}PEO_{14}$ membrane profile is consistent with there being less polymer in these membranes, than the 100% polymer membranes. The inner peaks of the SPA profile in Figure 6p could represent the hydrophobic/hydrophilic interface between the hydrophobic polybutadiene (PBd) and hydrophilic polyethylene oxide (PEO) blocks, while the outer peak may represent the center of the PEO corona.

2.7. Discussion

A fully extended PBd_{22}-PEO_{14} polymer is estimated to have a maximum bilayer thickness of ≈209 Å, and a hydrophobic core of 111 Å. Although polymers can form an extended, segregated

brush conformation, this conformation is entropically highly unfavorable. The polymer block chains can also collapse to protect the hydrophobic region,[26a] and the hydrophobic polymer chains can become entangled and interdigitate, thus decreasing the bilayer thickness.[40] Hence, the fully extended bilayer and hydrophobic core thickness provide physical limits for the underlying system. The collapsed polymer conformation can be modelled using a polymer random walk model (freely jointed chain), where the root mean squared end-to-end distance of the polymer is given by $\left\langle R^2 \right\rangle^{\frac{1}{2}} = N^{\nu-1}L$. Here N is the number of Kuhn segments, υ is the Flory exponent, and L is the polymer contour length. For polybutadiene, (1,2 addition), the Kuhn length is 13.7 Å,[41] while for poly ethylene oxide, the Kuhn length is 8 Å.[42] Under the assumption that the polymers are acting as ideal chains (similar to their configuration in a polymer melt) that do collapse and fully interdigitate, the Flory exponent is given by $\upsilon = 0.5$, leading to a bilayer thickness of 95 Å and hydrophobic core thickness of 55 Å for PBd_{22}-PEO_{14} membranes. However, this random walk model has to be used with great care as it is most accurate for the statistics of longer polymers, where the number of Kuhn segments, N, is much larger.

The peak-to-peak measurements from SAXS, cryo-ET, FFT and SPA profiles of 100 mol% $PBd_{22}PEO_{14}$ and thick 50 mol% $PBd_{22}PEO_{14}$ membranes can be compared with the theoretical values obtained from a polymer random walk model. The peak-to-peak values from all techniques are all below the predicted hydrophobic thickness for fully segregated polymer leaflets, but above the thickness calculated from fully interdigitated membranes (55 Å), suggesting PBd_{22}-PEO_{14} forms only partially interdigitating membranes.

SAXS appears more sensitive to the electron density at the center of the PEO hydrophilic corona and can collect data from the entire sample, approximately ranging from 10^{10}–10^{13} vesicles at once. However, the scattering pattern can be problematic to be modelled without a priori structural information.[25a] Cryo-ET and SPA images provide high contrast images with a large gradient in electron intensity at the hydrophilic–hydrophobic interface of the membranes, however the results are always specific with respect to the analyzed vesicles rather than representative of the whole sample. Therefore, SAXS remains an important characterization technique, when considering the ensemble structure in the sample.

The presence of thin and thick membrane populations in hybrid lipid-block copolymer vesicle samples might be interpreted as poor mixing between these components and a strong segregation into different vesicles. However, previous studies utilizing POPC and PBd_{22}-PEO_{14} have reported good mixing between these components into hybrid vesicles with a monomodal distribution of lipids and polymers centered around the sample mean.[15a] Giant unilamellar vesicles (GUVs), created by the electroformation method, have been studied containing a labelled polymer and lipid-like fluorescent probe, where these components were well mixed across 25 mol%, 50 mol% and 75 mol% components with a single broad distribution of relative fluorescence intensities across the giant unilamellar vesicle (GUV) population.[15a] Similarly, Lim et al. used flow cytometry of LUVs containing mixtures of POPC and PBd_{22}-PEO_{14} containing fluorescent lipid and polymer probes to show good mixing between these components in individual LUVs (formed by thin film rehydration and extrusion) in their samples.[16]

Assuming good mixing of lipid and polymer components between individual vesicles is given (with a monomodal relative distribution of components centered on the mean sample composition), a bistability in membrane structure between the thin and thick configurations is implied, dictated by the preferred structure of the lipids or the polymers. It can be inferred that membranes of intermediate structure between these two states are not energetically favorable and hence the vesicle selects a membrane structure in one of these two states upon formation. This might be driven by small differences in membrane composition within a well-mixed population, where thicker membranes are slightly enriched in block copolymer and vice-versa, or a bimodal distribution in the free energy distribution with respect to membrane thickness, where the difference in free energy between thick and thin membranes is small (or order $k_B T$). In the latter scenario, the homogeneity of the membrane structures in individual vesicles also implies that coexistence of these two membrane configurations in a single vesicle is also not energetically favoured, likely due to the line tension that would arise between these domains. A further potential interpretation is microphase separation of lipids and block copolymers into thick and thin membrane phases where the composition differences between the two phases is small. At present we do not favor this interpretation as we have not observed evidence for coexistence of these two phases in the same vesicle, which is commonly observed for phased separation in mixed vesicle systems. However further work to investigate the underlying mechanisms of the phenomenology reported in this study is warranted. These observations have interesting implications for the application of hybrid vesicles in biotechnology and nanomedicine, where two distinct membrane structures can coexist, which could give rise to differential vesicle properties in a single sample.

3. Conclusion

Generally, the membrane thickness was found to increase with increasing polymer fraction, from 52 Å for a pure lipid system to 97 Å for pure PBd_{22}-PEO_{14} vesicles. Overall, the bilayer thickness measurements from cryo-ET intensity profiles and SAXS EDPs for pure lipid and pure polymer membranes found in this investigation broadly corresponds with measurements determined previously by cryo-TEM,[24a] SAXS or SANS[37,43] and simulation.[26b] Here, the hydrophobic thickness of the membrane, previously under-considered in cryo-TEM membrane measurements,[24a,26] have been resolved using cryo-ET, as well as adding new details, including the presence of 2 bilayer populations in POPC/PBd_{22}-PEO_{14} hybrid samples, which has been utilized to optimize the SAXS model.

In 50 mol% and 75 mol% PBd_{22}-PEO_{14}/POPC hybrid vesicles, two thickness populations were found using cryo-ET: vesicles could be categorized by a visibly thick or thin membrane and homogeneity within these populations were confirmed using an automated analysis. SAXS confirms that the hybrid PBd_{22}-PEO_{14} samples comprise two populations: a thin

membrane with an EDP similar to a lipid bilayer and a thick membrane with an EDP similar to a pure polymer membrane. An FFT of the cryo-ET images also confirmed the peak positions found in the SAXS EDP.

SPA of 50 mol% PBd_{22}-PEO_{14} hybrid vesicles confirms a homogeneous distribution within a single vesicle. Previous literature has shown good mixing between these lipid and polymer components in hybrid membranes with a monomodal distribution of lipids and polymers between different vesicles centered on the mean composition. The cryo-EM and cryo-ET data also shows no evidence of phase separation into polymer-rich and lipid-rich domains within individual vesicles of hybrid samples. Together, this strongly implies a bistability between two membrane structures in coexisting vesicles of similar composition: thin membranes with a structure dictated by the preferred bilayer ordering of the lipids and thicker membranes with the membrane structure dictated by the partially interdigitated bilayer structure of the block copolymers. Intermediate membrane structures do not appear to be energetically favorable for these hybrid lipid-block copolymer blends. We also find that it is energetically unfavorable for domains of thin and thick membrane structures to coexist in the same vesicle, likely due to the high line tension of domain boundaries. As such, each vesicle selects between the lipid-like thin membrane structure or the polymer-like thick membrane structure during formation. This selection may be partially driven by differences in the relative vesicle compositions across the width of the monomodal mixing distribution of these components that has been previously reported.[15a,16]

These novel findings on the membrane structure of hybrid POPC/PBd_{22}-PEO_{14} vesicles have implications for their technological applications. For example, it is interesting to note that previous work inserting cytochrome bo_3 into these vesicle compositions finds that optimal stability of this enzyme's function is within 50 mol% PBd_{22}-PEO_{14} hybrid vesicles.[6b] Two distinct membrane structures exist at this composition: future work could investigate the distribution of these membrane proteins between thick and thin hybrid vesicle membrane populations and how each of these contribute to enzymatic function and stability. Different coexisting membrane populations will also have implications for the use of hybrid vesicles in drug delivery, where membrane thickness would influence the release kinetics of bioactive compounds. A distribution of release rates within a formulation might be beneficial for drug pharmacokinetics in some long-acting delivery applications.

4. Experimental Section

Materials: Diblock copolymers poly(butadiene-block-ethylene glycol) (PBd-b-PEO) with total molecular weights of 1800 g mol^{-1} were purchased from Polymer Source, Inc. (Montreal, Canada). PBd_{22}-PEO_{14} (PDI 1.01) had a hydrophobic butadiene block of 1200 g mol^{-1} (>85% 1,2 addition) and a hydrophilic ethylene glycol block of 600 g mol^{-1}. 1-palmitoyl-2-oleoyl-sn-glycero-3-phosphocholine (POPC) in chloroform was purchased from Avanti Polar Lipids (AL, USA) while protein A (10 nm colloidal gold) was purchased from Insight Biotechnology (Wembley, UK). Sodium chloride (NaCl), sodium hydroxide (NaOH) hydrogen peroxide and 4-(2-hydroxyethyl)-1-piperazine ethane sulfonic acid (HEPES) were bought from Thermo Fisher Scientific (Loughborough, Leicestershire, UK). Chloroform was purchased from VWR International Ltd. (Lutterworth, UK) and Filtered MilliQ water (filtered and deionized water 18.2 MΩ cm at 25 °C) was used for buffer and sample preparation.

LUV Formation: LUVs were prepared by the thin film rehydration and extrusion method. To generate different hybrid vesicle compositions, relative volumes of POPC (32 mM) and the polymer (6.57 mM) in chloroform were measured using a Hamilton syringe into a glass vial. The solutions were dried in a vacuum desiccator to give a lipid/polymer film and then rehydrated with 1.0 mL of aqueous solution of 40 mM HEPES and 20 mM sodium chloride buffered to pH 7.4 such that the final amphiphile concentration in all samples was 6.57 mM. The films were incubated at 50 °C for 5 min and vortexed for 1 min. The suspensions were then frozen in liquid nitrogen, thawed in a 60 °C water bath and vortexed for 10 s. This cycle was repeated 5 times. Suspensions were extruded 11 times at room temperature through 100 nm polycarbonate membrane filter using a LiposoFast Basic Extruder. The samples were then kept at 4 °C until further analysis. The size distributions of all vesicle samples were analyzed by dynamic light scattering using a Malvern Zetasizer Nano ZSP (Malvern Panalytical Ltd., Malvern, UK). Samples were diluted using the preparation buffer to 0.5 mM amphiphile concentration and were measured at 25 °C. The results from three independent repeat measurements were averaged.

SAXS at the Diamond Light Source: Samples were placed directly into quartz glass capillary tubes (0.01 mm wall thickness, 1.5 mm outer diameter) for measurement in the Diamond Light Source (Harwell Campus, Oxford, UK) I22 beamline at 17 keV with a sample to detector length of 6.7 m.[44] Scattering profiles were radially averaged and the capillary scattering as well as the background buffer profile was subtracted upon acquisition using the Diamond Light Source software, DAWN.[45] The q-calibrant was silver behenate. The scattering vector q covered a range of 0.01 to 0.27 $Å^{-1}$ ($q = 4\pi \sin(\theta)/\lambda$, with 2θ being the scattering angle and $\lambda = 0.7$ Å the X-ray wavelength). The vesicle scattering profiles were fitted using an in-house code running on MatLAB, which can be obtained by contacting the corresponding author.

Cryo-Electron Tomography: Protein A conjugated 10 nm gold nanoparticles (Insight Biotechnology) were used to act as fiducial markers when processing the tomograms. Gold fiducials were positively charged and need to be applied to the sample before the sample was applied to the grid. The markers were added following LUV formation. First the Protein A 10 nm gold solution was concentrated using a centrifuge (XG, 30 min) and re-suspended in a solution of 40 mM HEPES and 20 mM sodium chloride buffered to pH 7.4. 10 µL of suspended protein A was added to 10 µL of LUV sample. Copper Quantifoil grids (400 mesh, 2/2) were glow discharged for 33 s at 10 mA using a Cressington208 carbon coater. 3 µL of the samples were then placed directly on the grid which was blotted and vitrified using a FEI Vitrobot mk IV using a blot time of 6 s and a blot force of 6 at 4 °C and 100% relative humidity. The samples were kept under liquid nitrogen until required.

For cryoEM imaging, a FEI GII Titan Krios microscope with a Bioquantum K2 (Gatan) was used. Tilt series were collected using Tomo software with defocus set to 3 µm. The grids were exposed to an electron dose of 18 e^{-} $Å^{-2}$ s^{-1} and 61 images were taken at 2° increments and × 25 000 nominal magnification to create the tomogram. The final resolution for these images was 0.1855 pixel/Å.

The collection of images (movies) was motion corrected and tomograms were reconstructed with eTOMO software from the IMOD suite. Using protein A as the fiducial markers, the tomogram was aligned and applied with back projection and 10 iterations of SIRT to obtain a final reconstruction. Further analysis was carried out using FIJI software for bilayer measurements and a python code for phase determination.

Single Particle Analysis: In addition to cryo-ET and SAXS analysis on all PBd_{22}-PEO_{14} vesicle compositions, SPA was performed on 0%, 50%, and 100 mol% PBd_{22}-PEO_{14} sample to confirm the polymer membrane structure. Copper Quantifoil grids (400 mesh, 2 by 2 µm) were glow discharged for 33 s at 10 mA using a Cressington208 carbon coater. 0%, 50%, and 100 mol% PBd_{22}-PEO_{14} samples were then placed directly on the grid using a FEI Vitrobot mkIV using a blot time of 6 s and a blot

force of 6 at 4 °C and 100% relative humidity. Samples were vitrified using liquid ethane and were stored in liquid nitrogen until imaged. Samples were visualized using a FEI GII Titan Krios microscope equipped with a Falcon 4 DED and Selectris energy filter. Automated single particle data collection was carried out using EPU software (Version 2.11.0). Micrographs were collected at 105k with a pixel size of 1.2 Angstroms. An exposure time of 4.16 s gave a dose of 9.31 electrons per pixel per second, generating a total dose of 27 electrons per Angstroms^2 over 1001 EER frames. Micrographs were motion corrected using RELIONs own implementation and CTF estimated using CTFFind 4.1.

From these corrected micrographs particles were manually selected, extracted, and 2D classified. From the 2D projection images of 100 mol% PBd_{22}-PEO_{14} vesicles, images were grouped into three classes of 100 mol% PBd_{22}-PEO_{14} membrane section which were then combined to reconstruct a composite image of the membrane structures within the sample.

Analysis of Membrane Structure by SAXS: EDPs extracted from the SAXS fits were also used to determine bilayer thickness and hydrophobic core measurements. Bilayer thickness was measured using the peak-to-peak value while hydrophobic core borders were defined by the zero-point positions of the EDPs. As discussed also in the main text, differences EM- and SAXS-derived density profiles of the thick membrane vesicles do stem from the head-group fine-structure, as seen best in the SPA-data (Figure 6p). In this case, SAXS modelling was not able to reproduce the bi-modal density distribution of the head-group region in a statistically meaningful way (Section S9, Supporting Information).

Tomograms and SPA Images: Tomograms and composite images obtained by SPA were further analyzed using FIJI and OriginPro. Using FIJI, lines (5 pixels thickness) were always drawn from inside the lumen to the external buffer regions to differentiate the inner and outer leaflets in the final electron intensity profile. Per vesicle, at least 15 lines were drawn across the bilayer at various slices in a tomogram. The line profiles were adjusted on OriginPro to overlap at the central hydrophobic core, baseline corrected, averaged and normalized to give an electron intensity profile for each vesicle composition.

Membrane measurements of structural features in profiles from tomograms were taken: bilayer thickness was the full width half maximum (FWHM) between the baseline to the peak; and the hydrophobic core thickness was the peak-to-peak distance.

FFT of cryo-ET images were also obtained using FIJI software. The FFT images were smoothed using a Gaussian Blur function (radius 0.5) and a background subtraction with a rolling ball radius of 250 pixels was applied. The FFT image and contrast was then auto adjusted followed by applying a dark background threshold. The "Radial Profile Angle" plugin was then used to radially integrate the image from the center pixel, leading to a reciprocal space intensity function, analogous to a SAXS scattering profile. These profiles were fitted with the 3- and 4-Gaussian functions used to extract EDPs from SAXS data. The statistics of the total number of vesicles and number of independent tomograms used for each composition is given in Table S6, Supporting Information.

Automated Analysis Using Python of Tomography Images: Full description and mechanics of the code can be found in Ref. [33]. Briefly, the tomogram slices were first Canny filtered using FIJI. The apparent bilayer thickness was defined as the minimum distance between pixels on the inner and outer leaflet. Bilayer measurements from 20–30 images of each pure system were used to determine which observed distances in the hybrid compositions were categorized into polymer-like or lipid-like phases. The domains were mapped on to the individual tomograms of each hybrid vesicle composition by calculating the probability of each observed distance corresponding to either the polymer-like or lipid-like phase.

Statistical Analysis: For Figure 1g, the number of independent tomograms, vesicles, and line profiles per vesicle for each composition are given in Table S6, Supporting Information: in brief, between 4 and 8 independent tomograms with between 15 and 24 total vesicles and between 21 to 30 average line profiles per vesicle were used at each composition. For Figure 1h, the box plots show the range from the first to the third quartile (box), the median (line), and the range from the minimum to the maximum points (whiskers). In Figure 2, representative images of vesicles at selected composition are shown; overall, between 20 and 25 vesicles were analyzed for each hybrid composition: 25 mol% polymer (n = 20 thin membrane vesicles); 50 mol% polymer (n = 25, 15 thick membrane and 10 thin membrane); 75 mol% polymer (n = 24, 15 thick membrane and 9 thin membrane). For Figure 3c,d, n = 188 and n = 117 vesicles were analyzed for 50 mol% PBd_{22}-PEO_{14} and 75 mol% PBd_{22}-PEO_{14} compositions, respectively. Statistical significance for the presence of two distinct membrane thickness populations in 50 mol% PBd_{22}-PEO_{14} and 75 mol% PBd_{22}-PEO_{14} compositions, and for different vesicle sizes for thin and thick membranes were conducted using OriginPro software with a one-sided ANOVA (Tukey & Bonferroni) with $p < 0.05$ set as the threshold for significance. In Figure 6, the cryo-FFT data (Figure 6c,g,k,o) were averaged over between 9 and 14 vesicles from 3 independent tomograms for each composition (see Table S6, Supporting Information, for details). Also in Figure 6, the averaged SPA line profiles (Figure 6d,h,l,p) were taken from three independent image reconstructions were analyzed with a minimum of 10 line profiles taken per image and combined for each composition.

Supporting Information

Supporting Information is available from the Wiley Online Library or from the author.

Acknowledgements

R.S. acknowledges funding from the Engineering and Physical Sciences Research Council (EPSRC) as part of the Centre for Doctoral Training in Soft Matter and Functional Interfaces (SOFI CDT), grant number EP/L015536/1. L.J.C.J., M.R., and P.A.B. also acknowledge funding from the Biotechnology and Biological Sciences Research Council (BBSRC), grant number BB/T000546/1. The Titan Krios microscopes were funded by the University of Leeds (UoL ABSL award) and Wellcome Trust (108466/Z/15/Z). This work was carried out with the support of Diamond Light Source instrument I22 (proposals SM19127-1, SM18027-1 and SM22659-1), and the authors are particularly thankful to Arwen Tyler, Tim Snow, Andy Smith and Nick Terrill for their technical support during the beamtime.

Conflict of Interest

The authors declare no conflict of interest.

Data Availability Statement

The data that support the findings of this study are available from the corresponding author upon reasonable request.

Keywords

block copolymers, cryo-electron tomography, hybrid vesicles, membrane structures, single particle analysis, small angle X-ray scattering

Received: October 12, 2022
Revised: January 26, 2023
Published online: March 3, 2023

[1] J. W. Hindley, Y. Elani, C. M. McGilvery, S. Ali, C. L. Bevan, R. V. Law, O. Ces, *Nat. Commun.* **2018**, *9*, 1093.
[2] T. Huang, Z. Hou, Q. Xu, L. Huang, C. Li, Y. Zhou, *Langmuir* **2017**, *33*, 340.
[3] a) F. Meng, Z. Zhong, J. Feijen, *Biomacromolecules* **2009**, *10*, 197; b) R. Molinaro, C. Corbo, J. O. Martinez, F. Taraballi, M. Evangelopoulos, S. Minardi, I. K. Yazdi, P. Zhao, E. De Rosa, M. Sherman, *Nat. Mater.* **2016**, *15*, 1037; c) S. Khan, J. McCabe, K. Hill, P. A. Beales, *J. Colloid Interface Sci.* **2020**, *562*, 418.
[4] a) J.-L. Rigaud, B. Pitard, D. Levy, *Biochim. Biophys. Acta, Bioenerg.* **1995**, *1231*, 223; b) D. Papahadjopoulos, H. K. Kimelberg, *Prog. Surf. Sci.* **1974**, *4*, 141.
[5] P. A. Beales, S. Khan, S. P. Muench, L. J. C. Jeuken, *Biochem. Soc. Trans.* **2017**, *45*, 15.
[6] a) S. S. Hallan, P. Kaur, V. Kaur, N. Mishra, B. Vaidya, *Artif. Cells, Nanomed., Biotechnol.* **2016**, *44*, 334; b) S. Khan, M. Li, S. P. Muench, L. J. C. Jeuken, P. A. Beales, *Chem. Commun.* **2016**, *52*, 11020; c) E. Brodszkij, I. N. Westensee, S. F. Holleufer, C. Ade, P. D. D. Andres, J. S. Pedersen, B. Städler, *Appl. Mater. Today* **2022**, *29*, 101549; d) N. Hamada, S. Gakhar, M. L. Longo, *Biochim. Biophys. Acta, Bioenerg.* **2021**, *1863*, 183552; e) N. Marušič, L. Otrin, J. Rauchhaus, Z. Zhao, F. L. Kyrilis, F. Hamdi, P. L. Kastritis, R. Dimova, I. Ivanov, K. Sundmacher, *Proc. Natl. Acad. Sci. USA* **2022**, *119*, e2122468119; f) Y. K. Go, C. Leal, *Chem. Rev.* **2021**, *121*, 13996; g) J. F. Le Meins, C. Schatz, S. Lecommandoux, O. Sandre, *Mater. Today* **2013**, *16*, 397; h) E. Reimhult, M. M. Virk, *J. Biomed. Res.* **2021**, *35*, 301; i) D. Chen, M. M. Santore, *Soft Matter* **2015**, *11*, 2617.
[7] S. Majd, E. C. Yusko, Y. N. Billeh, M. X. Macrae, J. Yang, M. Mayer, *Curr. Opin. Biotechnol.* **2010**, *21*, 439.
[8] a) C. Hunte, *Biochem. Soc. Trans.* **2005**, *33*, 938; b) N. P. Barrera, M. Zhou, C. V. Robinson, *Trends Cell Biol.* **2013**, *23*, 1.
[9] a) H. Bermudez, A. K. Brannan, D. A. Hammer, F. S. Bates, D. E. Discher, *Macromolecules* **2002**, *35*, 8203; b) R. Seneviratne, S. Khan, E. Moscrop, M. Rappolt, S. P. Muench, L. J. C. Jeuken, P. A. Beales, *Methods* **2018**, *147*, 142; c) C. LoPresti, H. Lomas, M. Massignani, T. Smart, G. Battaglia, *J. Mater. Chem.* **2009**, *19*, 3576.
[10] a) J. S. Lee, J. Feijen, *J. Controlled Release* **2012**, *161*, 473; b) D. A. Christian, S. Cai, D. M. Bowen, Y. Kim, J. D. Pajerowski, D. E. Discher, *Eur. J. Pharm. Biopharm.* **2009**, *71*, 463.
[11] S. F. M. van Dongen, W. P. R. Verdurmen, R. J. R. W. Peters, R. J. M. Nolte, R. Brock, J. C. M. van Hest, *Angew. Chem. Int. Ed.* **2010**, *49*, 7213.
[12] H. Lomas, I. Canton, S. MacNeil, J. Du, S. P. Armes, A. J. Ryan, A. L. Lewis, G. Battaglia, *Adv. Mater.* **2007**, *19*, 4238.
[13] a) D. E. Discher, *Science* **2002**, *297*, 967; b) N. Muhammad, T. Dworeck, M. Fioroni, U. Schwaneberg, *J. Nanobiotechnol.* **2011**, *9*, 8.
[14] a) W. F. Paxton, P. T. McAninch, K. E. Achyuthan, S. H. R. Shin, H. L. Monteith, *Colloids Surf., B* **2017**, *159*, 268; b) L. Otrin, N. Marušič, C. Bednarz, T. Vidaković-Koch, I. Lieberwirth, K. Landfester, K. Sundmacher, *Nano Lett.* **2017**, *17*, 6816; c) C. Kleineberg, C. Wölfer, A. Abbasnia, D. Pischel, C. Bednarz, I. Ivanov, T. Heitkamp, M. Börsch, K. Sundmacher, T. Vidaković-Koch, *ChemBioChem* **2020**, *21*, 2149; d) R. Goers, J. Thoma, N. Ritzmann, A. Di Silvestro, C. Alter, G. Gunkel-Grabole, D. Fotiadis, D. J. Müller, W. Meier, *Commun. Chem.* **2018**, *1*, 35; e) S. Rottet, S. Iqbal, P. A. Beales, A. Lin, J. Lee, M. Rug, C. Scott, R. Callaghan, *Polymers* **2020**, *12*, 1049; f) M. L. Jacobs, M. A. Boyd, N. P. Kamat, *Proc. Natl. Acad. Sci. USA* **2019**, *116*, 4031; g) R. Catania, J. Machin, M. Rappolt, S. P. Muench, P. A. Beales, L. J. C. Jeuken, *Macromolecules* **2022**, *55*, 3415.
[15] a) R. Seneviratne, R. Catania, M. Rappolt, L. J. C. Jeuken, P. A. Beales, *Soft Matter* **2022**, *18*, 1294; b) R. Seneviratne, L. J. C. Jeuken, M. Rappolt, P. A. Beales, *Polymers* **2020**, *12*, 914.
[16] S. Lim, H.-P. De Hoog, A. Parikh, M. Nallani, B. Liedberg, *Polymers* **2013**, *5*, 1102.
[17] a) A. F. Barton, *CRC Handbook of Solubility Parameters and other Cohesion Parameters*, Routledge, New York, NY **2017**; b) A. F. Barton, *Handbook of Polymer-Liquid Interaction Parameters and Solubility Parameters*, CRC Press, Boca Raton, FL **1990**.
[18] C. Zaba, S. Ritz, C.-W. D. Tan, S. Zayni, M. Müller, U. Reuning, E.-K. Sinner, *ChemBioChem* **2015**, *16*, 1740.
[19] C. Magnani, C. Montis, G. Mangiapia, A. F. Mingotaud, C. Mingotaud, C. Roux, P. Joseph, D. Berti, B. Lonetti, *Colloids Surf., B* **2018**, *168*, 18.
[20] a) J. Nam, P. A. Beales, T. K. Vanderlick, *Langmuir* **2011**, *27*, 1; b) J. Nam, T. K. Vanderlick, P. A. Beales, *Soft Matter* **2012**, *8*, 7982.
[21] M. Kumar, J. E. O. Habel, Y.-X. Shen, W. P. Meier, T. Walz, *J. Am. Chem. Soc.* **2012**, *134*, 18631.
[22] A. Balestri, L. Chiappisi, C. Montis, S. Micciulla, B. Lonetti, D. Berti, *Langmuir* **2020**, *36*, 10941.
[23] a) M. Chemin, P.-M. Brun, S. Lecommandoux, O. Sandre, J.-F. L. Meins, *Soft Matter* **2012**, *8*, 2867; b) M. Fauquignon, E. Courtecuisse, R. Josselin, A. Mutschler, A. Brûlet, M. Schmutz, J.-F. L. Meins, *J. Colloid Interface Sci.* **2021**, *604*, 575.
[24] a) Y. Tahara, Y. Fujiyoshi, *Micron* **1994**, *25*, 141; b) P. M. Frederik, D. H. W. Hubert, *Methods Enzymol.* **2005**, *391*, 431; c) Y.-Y. Won, A. K. Brannan, H. T. Davis, F. S. Bates, *J. Phys. Chem. B* **2002**, *106*, 3354.
[25] a) J. S. Kim, B. Afsari, G. S. Chirikjian, *J. Comput. Biol.* **2017**, *24*, 13; b) A. Jiménez, S. Jonic, T. Majtner, J. Otón, J. L. Vilas, D. Maluenda, J. Mota, E. Ramírez-Aportela, M. Martínez, Y. Rancel, J. Segura, R. Sánchez-García, R. Melero, L. Del Cano, P. Conesa, L. Skjaerven, R. Marabini, J. M. Carazo, C. O. S. Sorzano, *Bioinformatics* **2019**, *35*, 2427.
[26] a) T. P. Smart, O. O. Mykhaylyk, A. J. Ryan, G. Battaglia, *Soft Matter* **2009**, *5*, 3607; b) M. Kowalik, A. B. Schantz, A. Naqi, Y. Shen, I. Sines, J. K. Maranas, M. Kumar, *RSC Adv.* **2017**, *7*, 54756.
[27] a) R. Nygaard, J. Kim, F. Mancia, *Curr. Opin. Struct. Biol.* **2020**, *64*, 26; b) M. R. Baker, G. Fan, I. I. Serysheva, *Eur. J. Transl. Myology* **2015**, *25*, 35; c) C. Sun, R. B. Gennis, *Chem. Phys. Lipids* **2019**, *221*, 114; d) M. Parmar, S. Rawson, C. A. Scarff, A. Goldman, T. R. Dafforn, S. P. Muench, V. L. Postis, *Biochim. Biophys. Acta, Bioenerg.* **2018**, *1860*, 378.
[28] E. J. Boekema, M. Folea, R. Kouřil, *Photosynth. Res.* **2009**, *102*, 189.
[29] a) M. R. Brzustowicz, A. T. Brunger, *J. Appl. Crystallogr.* **2005**, *38*, 126; b) N. Kučerka, J. F. Nagle, J. N. Sachs, S. E. Feller, J. Pencer, A. Jackson, J. Katsaras, *Biophys. J.* **2008**, *95*, 2356.
[30] C.-J. Su, S.-S. Wu, U. S. Jeng, M.-T. Lee, A.-C. Su, K.-F. Liao, W.-Y. Lin, Y.-S. Huang, C.-Y. Chen, *Biochim. Biophys. Acta, Bioenerg.* **2013**, *1828*, 528.
[31] a) A. Iglic, P. L. Perez, M. Rappolt, *Advances in Biomembranes and Lipid Self-Assembly*, Academic Press, Cambridge, MA **2019**; b) T. Kondela, P. Hrubovčák, D. Soloviov, D. Badreeva, T. Murugova, V. Skoi, A. Kuklin, O. Ivankov, N. Kučerka, *Soft Matter Systems for Biomedical Applications*, Springer, Berlin **2022**, p. 265.
[32] J. Wang, *Protein Sci.* **2017**, *26*, 1619.
[33] C. E. Cornell, A. Mileant, N. Thakkar, K. K. Lee, S. L. Keller, *Proc. Natl. Acad. Sci. USA* **2020**, *117*, 19713.
[34] J. Canny, *IEEE Trans. Pattern Anal. Mach. Intell.* **1986**, *PAMI-8*, 679.
[35] W. C. Poon, D. Andelman, *Soft Condensed Matter Physics in Molecular and Cell Biology*, CRC Press, Boca Raton, FL **2006**.
[36] a) G. Pabst, J. Katsaras, V. A. Raghunathan, M. Rappolt, *Langmuir* **2003**, *19*, 1716; b) P. Heftberger, B. Kollmitzer, F. A. Heberle, J. Pan, M. Rappolt, H. Amenitsch, N. Kučerka, J. Katsaras, G. Pabst, *J. Appl. Crystallogr.* **2014**, *47*, 173.
[37] G. Pabst, M. Rappolt, H. Amenitsch, P. Laggner, *Phys Rev E* **2000**, *62*, 4000.

[38] J. F. Nagle, S. Tristram-Nagle, *Biochim. Biophys. Acta, Rev. Biomembr.* **2000**, *1469*, 159.
[39] M. Rappolt, *J. Appl. Phys.* **2010**, *107*, 084701.
[40] G. Battaglia, A. J. Ryan, *J. Am. Chem. Soc.* **2005**, *127*, 8757.
[41] L. Fetters, D. Lohse, R. Colby, in *Physical Properties of Polymers Handbook*, Springer, Berlin **2007**, p. 447.
[42] W. W. Graessley, J. F. Douglas, *Phys. Today* **2005**, *58*, 64.
[43] N. Kučerka, M.-P. Nieh, J. Katsaras, *Biochim. Biophys. Acta, Bioenerg.* **2011**, *1808*, 2761.
[44] A. J. Smith, S. G. Alcock, L. S. Davidson, J. H. Emmins, J. C. H. Bardsley, P. Holloway, M. Malfois, A. R. Marshall, C. L. Pizzey, S. E. Rogers, O. Shebanova, T. Snow, J. P. Sutter, E. P. Williams, N. J. Terrill, *J. Synchrotron Radiat.* **2021**, *28*, 939.
[45] M. Basham, J. Filik, M. T. Wharmby, P. C. Y. Chang, B. El Kassaby, M. Gerring, J. Aishima, K. Levik, B. C. A. Pulford, I. Sikharulidze, D. Sneddon, M. Webber, S. S. Dhesi, F. Maccherozzi, O. Svensson, S. Brockhauser, G. Naray, A. W. Ashton, *J. Synchrotron Radiat.* **2015**, *22*, 853.